

RSC Applied Interfaces

Accepted Manuscript

This article can be cited before page numbers have been issued, to do this please use: Z. Wu, . Kubiszyn, K. Michalczewski, D. Smoczyski, P. Martyniuk and Y. Wu, *RSC Appl. Interfaces*, 2026, DOI: 10.1039/D6LF00119J.



This is an Accepted Manuscript, which has been through the Royal Society of Chemistry peer review process and has been accepted for publication.

Accepted Manuscripts are published online shortly after acceptance, before technical editing, formatting and proof reading. Using this free service, authors can make their results available to the community, in citable form, before we publish the edited article. We will replace this Accepted Manuscript with the edited and formatted Advance Article as soon as it is available.

You can find more information about Accepted Manuscripts in the [Information for Authors](#).

Please note that technical editing may introduce minor changes to the text and/or graphics, which may alter content. The journal's standard [Terms & Conditions](#) and the [Ethical guidelines](#) still apply. In no event shall the Royal Society of Chemistry be held responsible for any errors or omissions in this Accepted Manuscript or any consequences arising from the use of any information it contains.

Efficient Prediction of Effective Bandgap and Optical Absorption in InAs/InAsSb Type-II Superlattices Using Localization Landscape Theory

Zhi-Jie Wu¹, Łukasz Kubiszyn², Krystian Michalczewski², Dariusz Smoczyński², Piotr Martyniuk³, and Yuh-Renn Wu^{1*,4}

¹ Graduate Institute of Photonics and Optoelectronics and Department of Electrical Engineering, National Taiwan University, Taipei 10617, Taiwan

² VIGO Photonics S.A., 129/133 Poznańska Str., 05-850 Ożarów Mazowiecki, Poland

³ Institute of Applied Physics, Military University of Technology, 2 Kaliskiego St., 00-908 Warsaw, Poland

⁴ Center for Quantum Science and Engineering, National Taiwan University, Taipei 10617, Taiwan

(*Author to whom correspondence should be addressed: yrwu@ntu.edu.tw)

(Dated: 19 May 2026)

Ga-free InAs/InAsSb type-II superlattices (T2SLs) are promising absorber materials for mid-wave and long-wave infrared (MWIR and LWIR) photodetectors, yet quantitative modeling of their optically active bandgaps and absorption remains challenging due to strain and quantum confinement effects. In this work, the Localization Landscape (LL) theory is applied to efficiently predict effective bandgaps and optical absorption in strained InAs/InAsSb superlattices without explicitly solving the Schrödinger eigenvalue problem. The LL framework is coupled with strain-induced deformation potential theory to obtain effective quantum confinement potentials, from which absorption coefficients are directly evaluated. The calculated absorption spectra are quantitatively compared with absorption coefficients extracted from experimentally measured responsivity of MWIR and LWIR photodetectors. Excellent agreement is obtained in absorption onset energies, with LL-predicted optically active bandgaps matching Schrödinger-based calculations within an RMSE of 5.395 meV, and experimental cutoff energies within 5.502 meV. These results demonstrate that the LL framework serves as a computationally efficient and physically consistent alternative to eigenstate-based solvers for modeling disordered superlattice absorbers relevant to infrared photodetector design.

Keywords: Localization Landscape theory, Type-II superlattices, InAs/InAsSb, Optical absorption, Effective bandgap, photoconductors, RCWA

I. INTRODUCTION

Reducing size, cost, weight, and power consumption is a primary driver for modern infrared (IR) imaging development. This objective is best addressed through high operating temperature (HOT) photodetectors^{1–5}, which eliminate the need for bulky cryogenic cooling. However, achieving reliable HOT operation requires not only high crystalline quality but also modeling approaches capable of capturing the complex quantum and disorder effects inherent to nanoscale heterostructures. Ga-free InAs/InAsSb type-II superlattices (T2SLs) have recently attracted significant attention as an alternative to HgCdTe and conventional InAs/GaSb systems due to their long minority carrier lifetimes and highly tunable bandgap^{6–8}. By suppressing Ga-related native defects that act as Shockley–Read–Hall (SRH) recombination centres^{9–12}, these structures enable improved performance in the MWIR and LWIR spectral regimes¹³. In this work, we adopt the Localization Landscape (LL) theory coupled with the strain-induced deformation potentials as a unified and physically grounded framework to describe carrier confinement, effective bandgap, and optical absorption in strained InAs/InAsSb T2SLs. The LL approach provides effective quantum potentials for elec-

trons and holes without explicitly solving for eigenstates, naturally incorporating disorder-induced localization and quantum confinement effects^{14–17}. Within this framework, all effective bandgaps and absorption coefficients discussed in this study are extracted from the LL model. Selected Schrödinger-based eigenstate calculations are additionally employed for validation purposes, confirming the accuracy of the LL-based description while highlighting its substantial computational efficiency. Owing to its computational efficiency and physical transparency, the LL framework is well-suited for modeling optical absorption in InAs/InAsSb T2SLs while capturing essential quantum confinement and localization effects. In this study, the LL approach is employed to investigate the absorption characteristic of MWIR and LWIR InAs/InAsSb superlattice (SL) photodetectors and compare with experimental results in a wide spectrum range

II. DEVICE STRUCTURE AND EXPERIMENTAL METHODS

The studied cases include representative experimentally realized MWIR and LWIR SL absorbers with different layer thicknesses and antimony compositions, designed to capture the effects of strain, alloy disorder,



TABLE I. Structural parameters and cutoff wavelengths of InAs/InAsSb T2SL samples, ordered by their cutoff wavelength within each spectral range. Here, L_{contact} denotes the distance between the Au contacts.

	L-16.6	L-14.4	L-10.7	L-8.7	M-7	M-6
L_{InAs} (nm)	10.86	8.14	7.87	9.93	3.67	3.48
$L_{\text{InAs}_{1-y}\text{Sb}_y}$ (nm)	3.41	2.58	2.47	3.97	1.30	1.26
L_{contact} (mm)	2.43	2.36	1.97	1.72	2.77	3.09
y_{Sb}	0.42	0.44	0.38	0.30	0.35	0.335
λ_{cutoff} (μm)	16.56	14.44	10.66	8.71	6.98	5.98
T (K)	195	195	230	300	300	300
d_{GaAs} (mm)	1.1	1.1	1.1	1.1	0.5	0.5
d_{GaSb} (μm)	0.95	0.94	0.98	0.68	1.98	1.87
d_{SL} (μm)	2.86	3.10	3.95	2.97	2.66	2.55

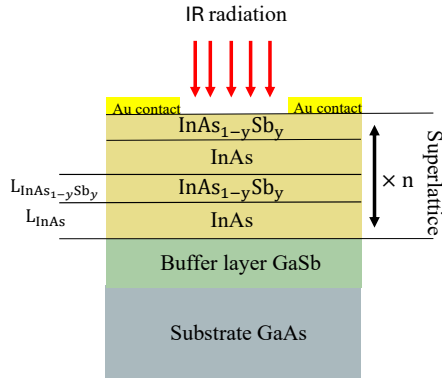


FIG. 1. Schematic illustration of the InAs/InAsSb T2SLs absorber structure investigated in this work. This thickness and composition are listed in Table I.

and quantum confinement, as schematically illustrated in Fig. 1. These structures serve as realistic platforms for evaluating the applicability of the LL framework under practical device conditions. The key structural parameters of the MWIR and LWIR SL absorbers investigated in this work are summarized in Table I. Here, d_{SL} denotes the total thickness of the superlattice absorber, λ_{cutoff} represents the cutoff wavelength defined as the wavelength at which the responsivity decreases to half of its maximum value, and d_{GaAs} denotes the thickness of the GaAs substrate.

The sample labels (L- z and M- z) indicate LWIR and MWIR designs, respectively, where the index z corresponds to the cutoff wavelength in micrometers rounded to one decimal place. For example, the sample labeled L-16.6 corresponds to a cutoff wavelength of 16.56 μm . The corresponding cutoff wavelengths are summarized in Table I.

In InAs/InAsSb T2SLs, the effective bandgap and cutoff wavelength can be tuned by adjusting the SL period and the Sb composition through strain-balanced design. Such band engineering is well established and forms the basis for MWIR and LWIR device optimization^{18–20}.

Based on these design considerations, the investigated structures were grown by molecular beam epitaxy

(MBE) using a RIBER Compact-21DZ system on semi-insulating GaAs (001) substrates. GaAs substrates were selected due to their lower cost, larger wafer availability, and mature growth technology compared to GaSb substrates. Although GaSb (001) substrates offer better lattice matching for antimonide-based superlattices, a GaSb buffer layer combined with an interfacial misfit (IMF) array was employed to accommodate the lattice mismatch, which has been shown to effectively mitigate the effects of lattice mismatch²¹.

To manage the significant lattice mismatch of approximately 7.8% between the GaAs substrate and the SL layers, a GaSb buffer layer utilizing an interfacial misfit (IMF) dislocation array was initially deposited. This IMF buffer serves as a high-quality virtual substrate. The InAs/InAsSb SLs were designed to be strain-balanced to the GaSb buffer. The individual SL layer thicknesses and the composition within the InAsSb layers were precisely engineered to ensure that the overall net lattice constant of the SL remained strain-balanced and closely matched to the underlying GaSb buffer, maintaining high structural integrity throughout the heterostructure was confirmed by the High-Resolution X-ray Diffraction (HRXRD) measurements shown in Fig. 10 in the Appendix section. Following the epitaxial growth, device fabrication was carried out through a simple processing sequence involving photoresist masking and the electrolytic deposition of Au contacts to form lateral photoconductors. For experimental characterization, the fabricated devices were mounted on thermoelectric coolers, and their spectral responsivity was measured using a spectrophotometer.

III. THEORETICAL MODEL AND SIMULATION FRAMEWORK

For this research, we employed an in-house one-dimensional Drift-Diffusion Charge-Control (1D-DDCC) solver to model the band structure and optical absorption of the strained InAs/InAsSb T2SL (Fig. 2). To analyze these properties, a simulation framework combining strain calculation, the Poisson and drift-diffusion equation, and the LL approach is adopted. Within this framework, strain effects on the electronic structure are described using deformation potential theory, as given in Eq.(1),

$$H_{\epsilon}^{\alpha\beta} = \sum_{i,j} D_{ij}^{\alpha\beta} \epsilon_{ij} \quad (1)$$

Here, α and β denote band indices corresponding to different electronic bands, and H_{ϵ} represents the strain-induced perturbation to the Hamiltonian. The coefficients $D_{ij}^{\alpha\beta}$ are the deformation potential constants associated with the strain tensor ϵ_{ij} .



$$\Delta E_c = a_c (\epsilon_{xx} + \epsilon_{yy} + \epsilon_{zz}), \quad (2)$$

$$\Delta E_{v,hh} = a_v (\epsilon_{xx} + \epsilon_{yy} + \epsilon_{zz}) + \frac{b}{2} (\epsilon_{xx} + \epsilon_{yy} - 2\epsilon_{zz}), \quad (3)$$

$$\Delta E_{v,lh} = a_v (\epsilon_{xx} + \epsilon_{yy} + \epsilon_{zz}) - \frac{b}{2} (\epsilon_{xx} + \epsilon_{yy} - 2\epsilon_{zz}), \quad (4)$$

where a_c and a_v are the conduction band and valence band deformation potential under hydrostatic pressure, respectively. b is the shear deformation potential. E_c and E_v are the conduction band and valence band potential before strain. $E'_{v,hh}$ and $E'_{v,lh}$ are the valence band potentials of heavy hole and light hole after strain, respectively, where the two bands are split.

The electrostatic potential ϕ is determined from the Poisson equation in Eq.(5), which describes the potential distribution arising from the local carrier and ionized dopant densities

$$\nabla \cdot (\epsilon_r \nabla \phi) = q(n - p + N_A^- - N_D^+), \quad (5)$$

where n and p are the electron and hole densities, and N_A^- and N_D^+ denote the ionized acceptor and donor densities, respectively. Here, ϵ_r is the dielectric permittivity of the material. Once the ϕ is obtained, E_c and E_v are parallel to $-q\phi$. The band offset issue will be treated in the program.

To calculate the effective bandgap in SL, the $k \cdot p$ model or single band Schrodinger solver is used to solve the eigenvalue and eigen wavefunctions. In Ref.²², Filoche et al. propose the LL model, and they proved that instead of solving the eigenvalues of $H\psi = E\psi$, the LL model solves $Hu = 1$. And $1/u$ can be denoted as effective quantum potentials. Details of the LL model can be found in Refs.^{15–17,23,24}. Hence, we can obtain the effective quantum potential by solving

$$\left(-\frac{\hbar^2}{2} \nabla \left(\frac{1}{m_e^*} \nabla \right) + (E_c + \Delta E_c) \right) u_e = 1, \quad (6)$$

$$\left(\frac{\hbar^2}{2} \nabla \left(\frac{1}{m_{hh}^*} \nabla \right) - (E_v + \Delta E_{v,hh}) \right) u_{hh} = 1, \quad (7)$$

$$\left(\frac{\hbar^2}{2} \nabla \left(\frac{1}{m_{lh}^*} \nabla \right) - (E_v + \Delta E_{v,lh}) \right) u_{lh} = 1, \quad (8)$$

where \hbar is the reduced Planck constant, m_e^* , m_{hh}^* , and m_{lh}^* are the electron, heavy hole, and light hole effective masses, respectively.

After obtaining $1/u$, the electron and hole densities are calculated in the energy domain using the Fermi–Dirac distribution functions $f_n(E, E_{fn})$ and $f_p(E, E_{fp})$, together with the corresponding density of states $N_{c,dos}(E)$ and $N_{v,dos}(E)$, as expressed in Eqs. (9) and (10) The quantities E_{fn} and E_{fp} represent the quasi-Fermi levels for electrons and holes, respectively.

$$n = \int_{-\infty}^{\frac{1}{u_e}} N_{c,dos}(E) \cdot f_n(E, E_{fn}) dE \quad (9)$$

$$p = \int_{-\infty}^{\frac{1}{u_{hh}}} N_{v,dos,hh}(E) \cdot f_p(E, E_{fp}) dE + \int_{-\infty}^{\frac{1}{u_{lh}}} N_{v,dos,lh}(E) \cdot f_p(E, E_{fp}) dE \quad (10)$$

The quasi-Fermi levels E_{fn} and E_{fp} are obtained by solving the drift–diffusion equations in Eqs. (11) and (12), where the electron and hole current densities are driven by the gradients of the quasi-Fermi levels. These current densities are then incorporated into the continuity equation in Eq.(13), which accounts for carrier transport under generation and recombination, where μ_n and μ_p are the electron and hole mobilities. G is the generation rate, and R is the total recombination rate.

$$J_n = n\mu_n \nabla E_{fn} \quad (11)$$

$$J_p = p\mu_p \nabla E_{fp} \quad (12)$$

$$\nabla \cdot J_{n,p} = -q(R - G) \quad (13)$$

After convergence of the coupled equations, the band profile and LL-derived effective quantum potentials are obtained, based on which the optical absorption coefficients $\alpha(\hbar\omega)$ are evaluated by considering transitions between the conduction and valence states. In Ref.²⁵, the author further prove that by treating the effective bandgap $E_g^{\text{eff}}(r) = \frac{1}{u_e(r)} - \frac{1}{u_h(r)}$, we can further obtain the absorption coefficient:

$$\alpha(\hbar\omega, E_g^{\text{eff}}) = \frac{1}{d_{SL}} \frac{2}{3} \frac{e^2 \hbar}{2m_0 \epsilon_0 c n_r} \int \frac{E_p \sqrt{2} m_r^{*3/2}}{\hbar\omega \pi^2 \hbar^3} \int \frac{1}{\sqrt{2\pi\sigma}} \exp\left(-\frac{(\hbar\omega - E)^2}{2\sigma^2}\right) \sqrt{E - E_g^{\text{eff}}(r)} dE dr \quad (14)$$

$\alpha(\hbar\omega)$ is the absorption coefficient obtained from the LL model. E_p is the material parameter related to the interband momentum matrix element. m_r^* is the reduced mass of the electron-hole system. ϵ_0 is the vacuum permittivity. m_0 is the free electron rest mass, and n_r is the real part of the refractive index of the material. c is the speed of light in vacuum. $\hbar\omega$ is the photon energy. Since the heavy hole band and light hole bands are split, the $\alpha_{\text{total}}(\hbar\omega)$ is further modified to

$$\alpha_{\text{total}}(\hbar\omega) = \alpha_{c-hh}(\hbar\omega, E_{g,c-hh}^{\text{eff}}) + \alpha_{c-lh}(\hbar\omega, E_{g,c-lh}^{\text{eff}}), \quad (15)$$

$$E_{g,c-hh}^{\text{eff}} = \left(\frac{1}{u_e} - \frac{1}{u_{hh}} \right), \quad (16)$$

$$E_{g,c-lh}^{\text{eff}} = \left(\frac{1}{u_e} - \frac{1}{u_{lh}} \right), \quad (17)$$



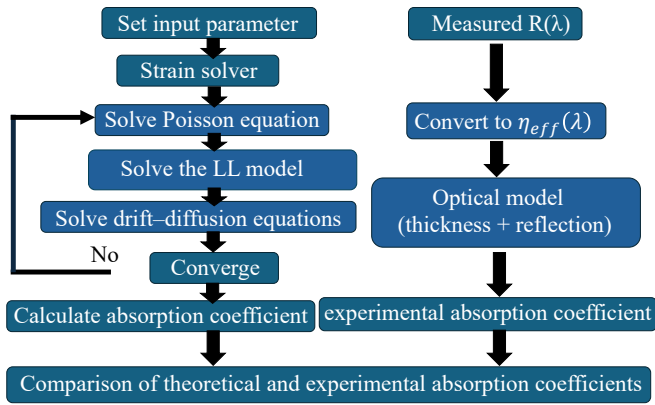


FIG. 2. Schematic illustration of the theoretical and experimental workflows used to extract and compare absorption coefficients. The left branch represents the simulation workflow of the coupled strain, Poisson, LL, drift-diffusion model, while the right branch shows the extraction procedure from measured responsivity.

where α_{c-hh} is the absorption coefficient from heavy hole band to conduction band. α_{c-lh} is the absorption coefficient from light hole band to conduction band. The Gaussian broadening is also considered in absorption calculation, where the broadening σ is used. Since the experimentally measured quantity is the responsivity, the absorption coefficient cannot be obtained directly. Therefore, the procedure illustrated in the right panel of Fig. 2 is adopted to convert the measured responsivity into the absorption coefficient for comparison with the LL model.

Since the investigated devices are photoconductors, the measured responsivity inherently includes the contribution of photoconductive gain²⁶, and can be expressed as

$$R(\lambda) = \frac{e\lambda}{hc} \eta(\lambda) \times g, \quad (18)$$

where $\eta(\lambda)$ is the quantum efficiency per incident photon absorbed and convert into electron-hole pair or we can call it as absorbance. g is the photoconductive gain, which converts the absorbed carrier into measured current density. Here, $R(\lambda)$ is the measured responsivity including photoconductive gain effects, h is Planck's constant, c is the speed of light in vacuum, and λ is the wavelength. Furthermore, $g = \frac{\tau}{t_t}$ is the photoconductive gain, where τ is free the carrier lifetime and t_t is the carrier transit time between ohmic contacts. The $\eta(\lambda)$ is related to the absorption coefficient, which can be written as

$$\eta(\lambda) = (1 - R_f) \left(1 - e^{-\alpha(\lambda)d_{SL}}\right) \times \frac{(1 + R_{b,eff} e^{-\alpha(\lambda)d_{SL}})}{1 - R_f R_{b,eff} e^{-2\alpha(\lambda)d_{SL}}} \quad (19)$$

where d_{SL} represents the physical thickness of the SL absorber. In the photon energy range below 0.7 eV, GaAs

and GaSb are assumed to be non-absorbing because the energy is below bandgap^{27–29}. And $\eta(\lambda) \times g$ represents the combined effect of carrier generation efficiency and photoconductive gain contributing to the photocurrent. R_f is the front-surface reflectance, and $R_{b,eff}$ is defined as the overall effective back-side reflectance seen by light transmitted through the superlattice toward the substrate side.

$$R_{b,eff} = R_{GaSb/GaAs} + \frac{(1 - R_{GaSb/GaAs})^2 R_{back}}{1 - R_{GaSb/GaAs} R_{back}} \quad (20)$$

In the present model, $R_{b,eff}$ accounts for the wavelength-dependent refractive indices at the GaSb/GaAs interface^{30–32}, as well as the non-ideal optical interface between the GaAs substrate and the silver paste attached to the thermoelectric cooler. The back-side reflectance, denoted as R_{back} , is defined as the reflectance associated with this non-ideal optical interface. Due to surface roughness, particle aggregation, and the non-continuous morphology of the silver paste³³, R_{back} is treated as an effective parameter and is reasonably assumed to be approximately 0.85. The correctness of Eq. (19) and Eq.(20) was verified using RCWA^{34,35}. In practice, however, the Fabry-Perot resonance predicted by RCWA was less pronounced, primarily due to surface roughness and non-ideal optical interfaces. Consequently, the measured absorbance spectrum more closely follows the averaged response, which is in better agreement with Eq. (19). Therefore, an effective reflectance parameter $R_{b,eff}$ was directly adopted in the fitting procedure.

A. Simulation Results of the LL Model

As an example, the LWIR L-8.7 structure is considered to illustrate the band profile obtained using the LL approach. As shown in Fig. 3, the strain-modified conduction band edge E'_c and valence band edges $E'_{v,hh}$ and $E'_{v,lh}$ are presented together with the corresponding effective quantum potentials $\frac{1}{u_e}$, $\frac{1}{u_{v,hh}}$, and $\frac{1}{u_{v,lh}}$ for electrons, heavy holes, and light holes, respectively.

The results exhibit the characteristic type-II band alignment of the InAs/InAs_{1-y}Sb_y SL, in which electrons are primarily confined within the InAs layers, while holes are mainly localized in the InAsSb layers, leading to a spatial separation of carriers. This behavior is clearly reflected in the landscape potentials: the electron effective potential $\frac{1}{u_e}$, shows relatively smooth spatial variation, indicating weaker confinement, whereas $\frac{1}{u_{v,hh}}$ and $\frac{1}{u_{v,lh}}$ exhibit pronounced localization within the InAs_{1-y}Sb_y regions, corresponding to stronger hole confinement.

The effective quantum potentials obtained by the LL model, providing direct insight into carrier localization and effective band-edge profiles without explicitly solving the Schrödinger equation. The SL period directly



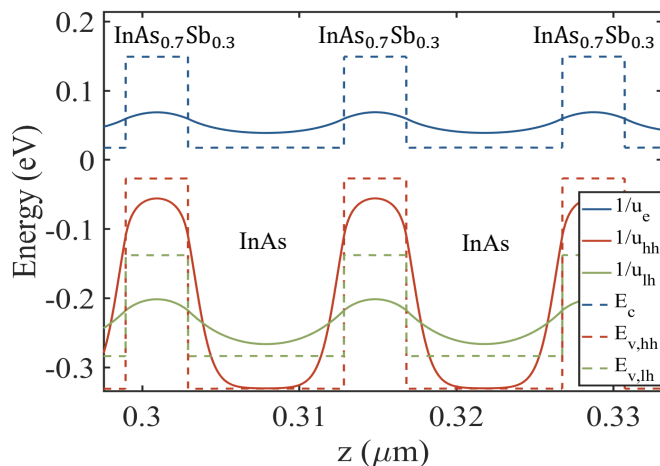


FIG. 3. The quantum potentials $1/u_e$, $1/u_{hh}$, and $1/u_{lh}$ represent the effective quantum potentials for electrons, heavy holes, and light holes, respectively.

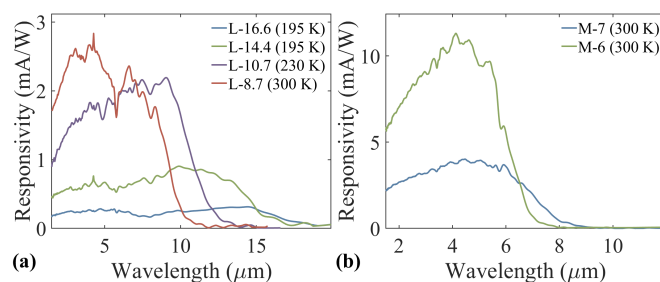


FIG. 4. Measured spectral responsivity of SL photodetectors. (a) LWIR devices and (b) MWIR devices, showing multiple experimental datasets within each spectral regime.

controls the effective bandgap through quantum confinement. In addition, the alloy composition of $\text{InAs}_{1-y}\text{Sb}_y$ influences both the band alignment and the strain distribution, thereby further modifying the band structure³⁶.

B. Experimental Responsivity

In the following analysis, we consider experimentally measured responsivity spectra from LWIR and MWIR photodetectors. The datasets are grouped by spectral regime to facilitate direct comparisons within each regime. The spectral responsivity of the fabricated devices is measured and summarized in Fig. 4(a) for the LWIR datasets and Fig. 4(b) for the MWIR datasets. Within each spectral regime, multiple experimental datasets are presented concurrently to enable systematic comparison of cutoff behavior. These experimentally measured spectra constitute the experimental basis for the subsequent extraction of absorption coefficients and quantitative comparison with theoretical models.

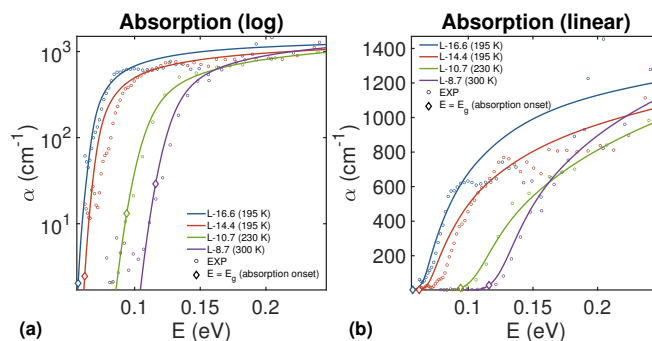


FIG. 5. Comparison of LWIR absorption coefficients between LL calculations and experiments shown on (a) logarithmic and (b) linear scales.

C. Comparison between Experimentally Extracted Absorption Coefficient and the LL Model

To establish a consistent and unambiguous basis for comparison, the experimental and theoretical absorption coefficients are obtained through two distinct and complementary procedures. The theoretical absorption coefficient is constructed within the LL framework using Eq.(14), which directly yields the optical absorption as a function of photon energy based on the effective bandgap landscape. All material parameters required for the LL-based absorption model, including the Kane energy and carrier effective masses, are summarized in Table III and I.(see Appendix). On the experimental side, the measured spectral responsivity $R(\lambda)$ is converted into the experimental absorption coefficient α_{ex} by numerically solving Eqs. (18) and (19). with the corresponding parameters summarized in Table III (see Appendix). By combining the material parameters (Tables II–III) with the geometric and structural properties of the InAs/InAsSb T2SL samples (Table I), the LL-predicted absorption coefficients can be directly compared with experimental results. The parameters used in the absorption coefficient calculations are listed in Table II and Table III. Most values are obtained by linear interpolation between InAs and InSb, while bowing terms are applied to electron affinity and bandgap to account for their nonlinear composition dependence. the g is required. At shorter wavelength, the absorption coefficient is larger, where the absorbance approaching the maximum can be expected.

The results are shown in Fig. 9. For longer wavelengths, where absorption is incomplete, the average g obtained from the shorter-wavelength regime is used to estimate α_{ex} . This approximation may influence the absolute magnitude of α_{ex} , but it does not affect the cutoff position of the absorption band edge

Figures 5 and 6 illustrate the direct comparison between the experimentally extracted absorption coefficients and the theoretical spectra calculated using LL framework for the LWIR and MWIR samples (see Ap-



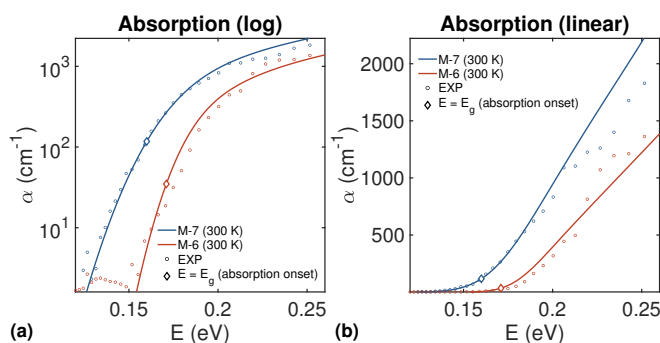


FIG. 6. Comparison of MWIR absorption coefficients between LL calculations and experiments shown on (a) logarithmic and (b) linear scales.

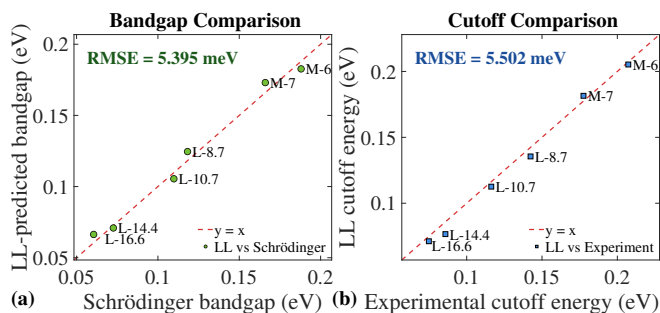


FIG. 7. Parity plots comparing the LL predictions with reference results: (a) bandgap versus Schrödinger calculations and (b) cutoff energy versus experiment, where the cutoff is defined at the half-maximum responsivity.

pendix for details of the methodology and validation). In both spectral ranges, the LL calculations exhibit band-edge (absorption-onset) features at energy positions consistent with the experimental results and capture the corresponding spectral evolution, supporting the use of the LL framework to describe the absorption behaviour near the band edge. The diamond markers denote the minimum bandgap energy E_g . The finite absorption observed for $E < E_g$ originates from Gaussian broadening of the band-edge transitions. To further validate the LL model, the LL-predicted cutoff energies were compared with the experimentally determined values. Fig. 7 illustrates the parity plot for the six representative samples, providing a visual assessment of the model's predictive accuracy.

As shown in Fig. 7(a), the LL-predicted bandgaps exhibit excellent agreement with the Schrödinger-based results, with a root-mean-square error (RMSE) of 5.395 meV. This confirms that the LL framework can accurately capture the minimum optically active transition energy across both LWIR and MWIR samples. The cutoff energy comparison in Fig. 7(b), defined using the half-maximum responsivity criterion, also demonstrates good agreement, with an RMSE of 5.502 meV. For consistency, the cutoff energy of the LL results is extracted by first converting the LL-derived absorption coefficient

into the corresponding optical response and subsequently identifying the energy at half of the maximum responsivity. A slightly larger deviation is observed in the MWIR region, which can be attributed to the sharper spectral drop near the cutoff, making the extracted cutoff energy more sensitive to variations in spectral shape. Overall, these results demonstrate the robustness of the LL framework in accurately predicting both the effective bandgap and the device-level optical response.

IV. CONCLUSION

In this work, the LL framework was applied to analyze optical absorption in MWIR and LWIR InAs/InAsSb T2SL absorbers. Within the effective-mass approximation, the LL formalism provided physically transparent effective band landscapes that capture carrier localization and band-edge formation without solving the full Schrödinger equation. Direct comparison with experimentally extracted absorption coefficients confirmed that the LL model reproduces both the spectral evolution and the absorption onset across a broad IR range. Quantitative validation showed excellent agreement: the LL-predicted bandgaps matched Schrödinger calculations with an RMSE of 5.395 meV, while cutoff energies agreed with experiment within 5.502 meV. These results demonstrate that the LL framework provides a computationally efficient and physically consistent alternative to eigenstate-based solvers, enabling robust modeling of disordered superlattice absorbers and serving as a practical tool for the design and optimization of large-scale infrared photodetectors.

ACKNOWLEDGMENT

This work is supported by NSTC under grant 112-2923-E-002-008-MY3, 114-2622-8-002-016, 115-2119-M-002-003, and 112-2221-E-002-215-MY3. Prof. Yuh-Renn Wu is also supported by the Leap fellowship of the Foundation for the Advancement of Outstanding Scholarship. This work was also supported by the Polish National Centre for Research and Development grant POLTAJ10/2022/37/LWIRPSBDA/2023.

V. APPENDIX

A. Material and optical parameters

The material and optical parameters used in this work are summarized in Table II and Table III. The refractive index, front-surface reflectance, Kane energy E_p , lattice constant, and deformation potential parameters of $\text{InAs}_{1-y}\text{Sb}_y$ are treated as composition-dependent quantities obtained through linear interpolation between the corresponding binary compounds.



TABLE II. Material parameters of the binary endpoints used in the calculations^{41–43}

Parameter	InAs	InSb
a (Å)	6.058	6.479
a_c (eV)	-5.08	-6.94
a_v (eV)	-1.0	-0.36
b (eV)	-1.8	-2.0
χ (eV)	4.9	4.59
m_e (m_0)	0.027	0.014
$m_{hh,z}$ (m_0)	0.3333	0.2632
$m_{hh,\parallel}$ (m_0)	0.0351	0.0199
$m_{lh,z}$ (m_0)	0.027	0.0152
$m_{lh,\parallel}$ (m_0)	0.087	0.0518
E_p (eV)	21.5	23.3
n	3.4	4.0
bandgap bowing term $b_{Eg} = 0.67$ eV		
electron affinity bowing term $b_\chi = -0.2262$ eV		

TABLE III. Sample-specific parameters, including Sb composition, temperature, Gaussian broadening, and band edge shifts.

Sample	y_{Sb}	T (K)	σ (eV)	ΔE_c (eV)	$\Delta E_{v,hh}$ (eV)	$\Delta E_{v,lh}$ (eV)
L-16.6	0.42	195	$0.18 k_B T$	0.1041	0.0728	-0.1024
L-14.4	0.44	195	$0.18 k_B T$	0.1114	0.0775	-0.1084
L-10.7	0.38	230	$0.4 k_B T$	0.09	0.0633	-0.0904
L-8.7	0.30	300	$0.45 k_B T$	0.0629	0.0449	-0.066
M-7	0.35	300	$0.45 k_B T$	0.0796	0.0563	-0.0813
M-6	0.335	300	$0.45 k_B T$	0.0745	0.0529	-0.0767

The effective masses are evaluated using inverse linear interpolation between the binary endpoints and are applied to all band components. In zincblende structures, the in-plane directions are isotropic, and thus the in-plane effective masses are taken as $m_{hh,\parallel} = m_{hh,x} = m_{hh,y}$ and $m_{lh,\parallel} = m_{lh,x} = m_{lh,y}$.

For the InAsSb alloy, key band parameters, including the electron affinity and the bandgap, are composition dependent and exhibit non-linear behavior due to alloy effects³⁷. In this work, these quantities are described using bowing-type interpolation expressions:

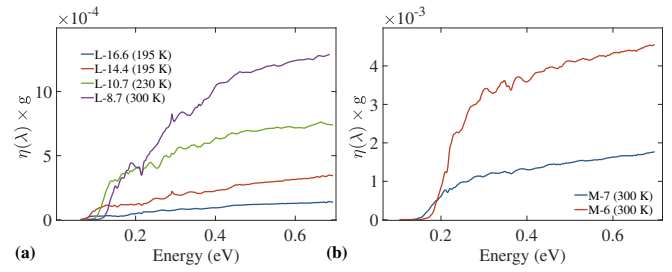
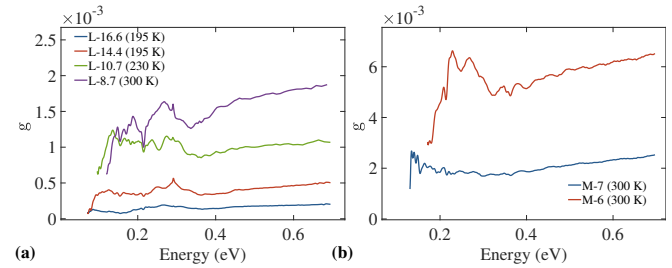
$$\chi(y) = \chi_{\text{InSb}} \cdot y + \chi_{\text{InAs}}(1 - y) - b_\chi y(1 - y) \quad (21)$$

$$E_g(y) = E_{g,\text{InSb}} \cdot y + E_{g,\text{InAs}}(1 - y) - b_{E_g} y(1 - y) \quad (22)$$

where $E_g(y)$ and $\chi(y)$ denote the bandgap and electron affinity of $\text{InAs}_{1-y}\text{Sb}_y$, respectively, $E_{g,\text{InAs}}$ and $E_{g,\text{InSb}}$ are the bandgaps of the binary compounds, χ_{InAs} and χ_{InSb} are the corresponding electron affinities, and b_{E_g} and b_χ are the associated bowing parameters.

In addition, Gaussian broadening is used to account for thermal effects and disorder-induced band-edge smearing^{38,39}, where the broadening width σ is taken to be proportional to temperature⁴⁰.

E'_c , $E'_{v,hh}$, and $E'_{v,lh}$ in the above table represent the strain-induced shifts of the conduction band and valence band edges at the Γ point, where the strain is defined with respect to the GaSb buffer layer.

FIG. 8. $\eta(\lambda) \times g$ as a function of photon energy for (a) LWIR and (b) MWIR devices.FIG. 9. Extracted g of the MWIR and LWIR samples by assuming the absorption coefficient calculated by the LL model is accurate.

The experimental $\eta(\lambda) \times g$ spectra shown in Fig. 8 were obtained from the measured responsivity using Eq. (18), followed by wavelength-to-energy conversion. To extract the absorption coefficient, however, the gain must first be determined, and then η and α can be obtained using Eq. (19). A condition where the gain is independent of the absorption coefficient arises when the absorption is sufficiently strong to reach the maximum η . This maximum occurs when all incident light is absorbed before reflection from the back reflector. For example, in the M-7 case, $\eta(\lambda) \times g$ begins to saturate for $\hbar\omega > 0.3$ eV. The maximum absorption can be expressed as

$$\eta_{\text{max}} = (1 - R_f), \quad (23)$$

where most incident light is absorbed. Hence, the gain can be estimated near $\hbar\omega = 0.3$ eV, and this value may be assumed to apply for $\hbar\omega < 0.3$ eV to obtain the absorption coefficient in that regime.

To further verify this, Fig. 9 shows the calculated gain obtained by using the absorption coefficient calculated by the LL model.

As shown in Fig. 9, above the absorption saturation region, the gain is smooth and slightly increases as $\hbar\omega$ increases. This increase may be attributed to improved carrier extraction, since absorbed carriers are closer to the surface and the contact. Therefore, a representative value of g is obtained by averaging g over a selected energy window near the onset of the saturation region. This averaged value is then used as the effective gain of the device to extract the absorption coefficient below the saturation region. The oscillations observed below satu-



ration may be due to a weak Fabry–Perot mode. Using this obtained gain, g , the experimental absorption coefficient is determined by numerically inverting Eq.(19). The resulting absorption spectra are presented in Fig. 5 and Fig. 6.

Since the photoconductive gain is defined as $g = \frac{\tau}{t_p}$, different combinations of $\eta(\lambda)$ and g can produce similar responsivity spectra. Thus, measured responsivity mainly reflects the combined quantity $\eta(\lambda) \times g$. Even if the carrier continuity equations are solved self-consistently, transport and recombination parameters must still be assumed or fitted. Consequently, $\eta(\lambda)$ and photoconductive gain cannot be uniquely separated from responsivity or $\eta(\lambda) \times g$ spectra alone, except in the regime above the saturation region where separation becomes possible.

B. HRXRD characterization

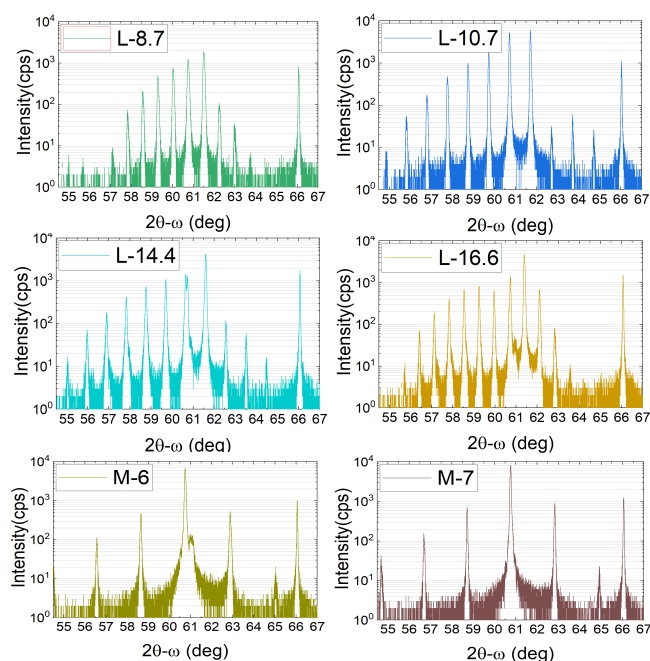


FIG. 10. High-resolution X-ray diffraction (HRXRD) 2θ - ω scans of the investigated LWIR and MWIR InAs/InAsSb superlattice samples.

All investigated samples exhibit clear superlattice satellite peaks in the HRXRD 2θ - ω scans, indicating good periodicity and interface quality of the InAs/InAsSb superlattices. The well-defined higher-order diffraction peaks further suggest relatively uniform layer thicknesses and good structural coherence throughout the absorber region.

VI. REFERENCES

- J. Jiang, K. Liu, L. Zhou, Y. Zhao, R. Li, T. Li, D. Wu, G. Wang, D. Jiang, H. Hao, Y. Xu, and Z. Niu, "InAs/InAsSb type-II superlattice mid-wavelength infrared photodetectors with high antimony component absorber quantum efficiency enhancement," *Journal of Crystal Growth* **666**, 128228 (2025).
- S. A. Pour, E. K. Huang, G. Chen, A. Haddadi, B.-M. Nguyen, and M. Razeghi, "High operating temperature midwave infrared photodiodes and focal plane arrays based on type-II InAs/GaSb superlattices," *Applied Physics Letters* **98**, 143501 (2011).
- A. Rogalski, M. Kopytko, W. Hu, and P. Martyniuk, "Infrared HOT photodetectors: status and outlook," *Sensors* **23**, 7564 (2023).
- A. Rogalski, M. Kopytko, F. Dai, R. Jiang, F. Wang, W. Hu, and P. Martyniuk, "Infrared HOT material systems vs. Law 19 paradigm," *Measurement* **230**, 114495 (2024).
- X. Xue, M. Chen, Y. Luo, T. Qin, X. Tang, and Q. Hao, "High-operating-temperature mid-infrared photodetectors via quantum dot gradient homojunction," *Light: Science & Applications* **12**, 2 (2023).
- J. Jiang, G. Wang, D. Wu, Y. Xu, F. Chang, W. Zhou, N. Li, D. Jiang, H. Hao, S. Cui, *et al.*, "High-performance infrared photodetectors based on InAs/InAsSb/AlAsSb superlattice for 3.5 μm cutoff wavelength spectra," *Optics Express* **30**, 38208–38215 (2022).
- B. C. Connelly, G. D. Metcalfe, H. Shen, and M. Wraback, "Direct minority carrier lifetime measurements and recombination mechanisms in long-wave infrared type II superlattices using time-resolved photoluminescence," *Applied physics letters* **97**, 251117 (2010).
- A. Rogalski, " α /G figure of merit for infrared photodetector materials," *Journal of Applied Physics* **137**, 170701 (2025).
- E. Steenbergen, B. Connelly, G. Metcalfe, H. Shen, M. Wraback, D. Lubyshev, Y. Qiu, J. Fastenau, A. Liu, S. Elhamri, *et al.*, "Significantly improved minority carrier lifetime observed in a long-wavelength infrared III-V type-II superlattice comprised of InAs/InAsSb," *Applied Physics Letters* **99**, 251110 (2011).
- G. Cao, *Nanostructures & nanomaterials: synthesis, properties & applications* (Imperial college press, 2004).
- B. Liu, L. Zhu, Y. Liu, L. Lu, R. Gong, H. An, D. Zhang, X. Zheng, Y. Feng, and M. Dong, "Temperature dependent growth of InAs/InAsSb superlattices by molecular beam epitaxy for HOT mid-wavelength infrared detectors," *Materials Science in Semiconductor Processing* **163**, 107590 (2023).
- Y. Zhang, Y. Shan, F. Chang, Y. Liang, X. Zhang, G. Wang, D. Wu, D. Jiang, H. Hao, Y. Xu, *et al.*, "Improvement of mid-wavelength InAs/InAsSb nBn infrared detectors performance through interface control," *Infrared Physics & Technology* **143**, 105619 (2024).
- M. Kopytko, G. Kołodziej, P. Baranowski, K. Murawski, Ł. Kubiszyn, K. Michalczewski, B. Seredyński, K. Szlachetko, J. Jureńczyk, and W. Gawron, "LWIR InAs/InAsSb Superlattice Detector for Cooled FPA," in *Proceedings*, Vol. 129 (MDPI, 2025) p. 28.
- D. N. Arnold, G. David, D. Jerison, S. Mayboroda, and M. Filoche, "Effective confining potential of quantum states in disordered media," *Physical review letters* **116**, 056602 (2016).
- M. Filoche, M. Piccardo, Y.-R. Wu, C.-K. Li, C. Weisbuch, and S. Mayboroda, "Localization landscape theory of disorder in semiconductors. I. Theory and modeling," *Physical Review B* **95**, 144204 (2017).
- C.-K. Li, M. Piccardo, L.-S. Lu, S. Mayboroda, L. Martinelli, J. Peretti, J. S. Speck, C. Weisbuch, M. Filoche, and Y.-R. Wu, "Localization landscape theory of disorder in semiconductors. III. Application to carrier transport and recombination in light emitting diodes," *Physical Review B* **95**, 144206 (2017).
- M. Piccardo, C.-K. Li, Y.-R. Wu, J. S. Speck, B. Bonef, R. M. Farrell, M. Filoche, L. Martinelli, J. Peretti, and C. Weisbuch,



- “Localization landscape theory of disorder in semiconductors. II. Urbach tails of disordered quantum well layers,” *Physical Review B* **95**, 144205 (2017).
- ¹⁸D. Z. Ting, S. B. Rafol, A. Khoshakhlagh, A. Soibel, S. A. Keo, A. M. Fisher, B. J. Pepper, C. J. Hill, and S. D. Gunapala, “InAs/InAsSb Type-II Strained-Layer Superlattice Infrared Photodetectors,” *Micromachines* **11** (2020), 10.3390/mi11110958.
- ¹⁹J. A. Keen, D. Lane, M. Kesaria, A. R. J. Marshall, and A. Krier, “InAs/InAsSb type-II strained-layer superlattices for mid-infrared LEDs,” *Journal of Physics D: Applied Physics* **51**, 075103 (2018).
- ²⁰L. K. Casias, C. P. Morath, E. H. Steenbergen, G. A. Umanamembreno, P. T. Webster, J. V. Logan, J. K. Kim, G. Balakrishnan, L. Faraone, and S. Krishna, “Vertical carrier transport in strain-balanced InAs/InAsSb type-II superlattice material,” *Applied Physics Letters* **116**, 182109 (2020).
- ²¹D. Kwan, M. Kesaria, J. Jiménez, V. Srivastava, M. Delmas, B. Liang, F. Morales, and D. Huffaker, “Monolithic integration of a 10 μm cut-off wavelength InAs/GaSb type-II superlattice diode on GaAs platform,” *Scientific Reports* **12**, 11616 (2022).
- ²²M. Filoche and S. Mayboroda, “Universal mechanism for Anderson and weak localization,” *Proceedings of the National Academy of Sciences* **109**, 14761–14766 (2012).
- ²³T.-Y. Tsai, K. S. Qwah, J.-P. Banon, M. Filoche, C. Weisbuch, Y.-R. Wu, and J. S. Speck, “Carrier localization in III-nitride versus conventional III-V semiconductors: A study on the effects of alloy disorder using landscape theory and the Schrödinger equation,” *Phys. Rev. Appl.* **20**, 044069 (2023).
- ²⁴H.-C. Huang, S.-M. Chen, C. Weisbuch, J. S. Speck, and Y.-R. Wu, “The influence of V-defects, leakage, and random alloy fluctuations on the carrier transport in red InGaN MQW LEDs,” *Applied Physics Reviews* **12**, 031402 (2025).
- ²⁵J.-P. Banon, P. Pelletier, C. Weisbuch, S. Mayboroda, and M. Filoche, “Wigner-Weyl description of light absorption in disordered semiconductor alloys using the localization landscape theory,” *Physical Review B* **105**, 125422 (2022).
- ²⁶G. Ariyawansa, M. Grupen, J. M. Duran, J. E. Scheihing, T. R. Nelson, and M. T. Eismann, “Design and modeling of InAs/GaSb type II superlattice based dual-band infrared detectors,” *Journal of Applied Physics* **111**, 073107 (2012).
- ²⁷M. Wasiak, M. Motyka, T. Smolka, J. Ratajczak, and A. Jasik, “Absorption and dispersion in undoped epitaxial GaSb layer,” *Materials Research Express* **5**, 025907 (2018).
- ²⁸C. Ghezzi, R. Magnanini, A. Parisini, B. Rotelli, L. Tarricone, A. Bosacchi, and S. Franchi, “Optical absorption near the fundamental absorption edge in GaSb,” *Physical Review B* **52**, 1463 (1995).
- ²⁹M. Sturge, “Optical absorption of gallium arsenide between 0.6 and 2.75 eV,” *Physical Review* **127**, 768 (1962).
- ³⁰S. Adachi, “Optical dispersion relations for GaP, GaAs, GaSb, InP, InAs, InSb, $\text{Al}_x\text{Ga}_{1-x}\text{As}$, and $\text{In}_{1-x}\text{Ga}_x\text{As}_y\text{P}_{1-y}$,” *Journal of Applied Physics* **66**, 6030–6040 (1989).
- ³¹A. D. Rakić and M. L. Majewski, “Modeling the optical dielectric function of GaAs and AlAs: Extension of Adachi’s model,” *Journal of Applied Physics* **80**, 5909–5914 (1996).
- ³²D. F. Edwards and R. H. White, “Gallium Antimonide (GaSb),” in *Handbook of Optical Constants of Solids*, edited by E. D. Palik (Academic Press, 1997) pp. 597–606.
- ³³M. Dehghani and C. David, “Light Scattering from Rough Silver Surfaces: Modeling of Absorption Loss Measurements,” *Nanomaterials* **11** (2021), 10.3390/nano11010113.
- ³⁴C.-H. Hsieh, J.-Y. Huang, and Y.-R. Wu, “Analysis of two-terminal perovskite/silicon tandem solar cells with differing texture structure, perovskite carrier lifetime, and tunneling junction quality,” *Journal of Applied Physics* **135**, 115002 (2024).
- ³⁵H.-Y. Wang, H. Lee, P. Martyniuk, and Y.-R. Wu, “Dielectric resonator antenna-coupled T2SL cascades for LWIR enhancement,” *Japanese Journal of Applied Physics* (2026), 10.35848/1347-4065/ae6d61.
- ³⁶T. Manyk, K. Michalczewski, K. Murawski, P. Martyniuk, and J. Rutkowski, “InAs/InAsSb strain-balanced superlattices for longwave infrared detectors,” *Sensors* **19**, 1907 (2019).
- ³⁷T. Manyk, K. Murawski, K. Michalczewski, K. Grodecki, J. Rutkowski, and P. Martyniuk, “Method of electron affinity evaluation for the type-2 InAs/InAs $_{1-x}$ Sb $_x$ superlattice,” *Journal of Materials Science* **55**, 5135–5144 (2020).
- ³⁸A. Canul, I. Lukman, and L. Bergman, “The Gaussian nature of the band-edge of ZnO microcrystalline thin films,” *AIP Advances* **12**, 125201 (2022).
- ³⁹R. A. Redkin, N. I. Onishchenko, A. V. Kosobutsky, V. N. Brudnyi, X. Su, and S. Y. Sarkisov, “Temperature-Dependent Optical Absorption and DLTS Study of As-Grown and Electron-Irradiated GaSe Crystals,” *Crystals* **15**, 372 (2025).
- ⁴⁰C. Grein and S. John, “Temperature dependence of the Urbach optical absorption edge: A theory of multiple phonon absorption and emission sidebands,” *Physical Review B* **39**, 1140 (1989).
- ⁴¹S. Adachi, *Properties of semiconductor alloys: group-IV, III-V and II-VI semiconductors* (John Wiley & Sons, 2009).
- ⁴²P. Paskov, “Refractive indices of InSb, InAs, GaSb, InAs $_x$ Sb $_{1-x}$, and In $_{1-x}$ Ga $_x$ Sb: effects of free carriers,” *Journal of applied physics* **81**, 1890–1898 (1997).
- ⁴³I. Vurgaftman, J. R. Meyer, and L. R. Ram-Mohan, “Band parameters for III–V compound semiconductors and their alloys,” *Journal of applied physics* **89**, 5815–5875 (2001).



Data Availability Statement

View Article Online
DOI: 10.1039/D6LF00119J

All input files used in the simulations are available from the corresponding author upon reasonable request. The simulation software employed in this study can be downloaded from the corresponding author's group website at <https://yrwu-wk.ee.ntu.edu.tw/index.php/download-ntu-itri-ddcc/>.

